# Polarimetric Wireless Indoor Channel Modelling Based on Propagation Graph

Ramoni Adeogun, Troels Pedersen, Carl Gustafson and Fredrik Tufvesson

***Abstract*—This paper generalizes a propagation graph model to polarized indoor wireless channels. In the original contribution, the channel is modelled as a propagation graph in which vertices represent transmitters, receivers and scatterers while edges represents the propagation conditions between vertices. Each edge is characterized by an edge transfer function accounting for the attenuation, delay spread and phase shift on the edge. In this contribution, we extend this modelling formalism to polarized channels by incorporating depolarization effects into the edge transfer functions and hence, the channel transfer matrix. We derive closed form expressions for the polarimetric power delay spectrum and cross-polarization ratio of the indoor channel. The expressions are derived considering average signal propagation in a graph and relate these statistics to model parameters, thereby providing a useful approach to investigate the averaged effect of these parameters on the channel statistics. Furthermore, we present a procedure for calibrating the model based on method of moments. Simulations were performed to validate the proposed model and the derived approximate expressions using both synthetic data and channel measurements at 15 GHz and 60 GHz. We observe that the model and approximate expressions provide good fits to the measurement data.**

***Index Terms*—Directed graph, polarization, MIMO system, stochastic channel model, dual polarized system, millimetre wave, measurements, propagation graph**

## I. Introduction

UTILIZATION of the additional degrees of freedom offered by polarization in wireless propagation to increase channel spectral efficiency has received considerable attention within the last several years. For example, in MIMO systems, antenna elements having dual polarizations offer significant increase in channel capacity and often require less space for deployment than those with single polarization [1], [2]. More recently, collocated dual-polarized antennas have been identified as a cost- and space-effective configuration in MIMO deployments and have been adopted as the antenna configuration of choice in the 3GPP, LTE and LTE-Advanced. It is also expected that polarization will be an integral part of future generation wireless communication techniques such as millimeter wave propagation [3] and massive MIMO systems [4].

Exploiting the full benefits of polarized systems requires adequate understanding of the polarized wireless propagation channels. A common practice in design and performance evaluation of wireless communication systems is therefore, to use mathematical models for characterizing the propagation channel. In addition to temporal, frequency and directional properties in classical channel models, models for polarized channels must incorporate polarization and depolarization effects arising from reflection, diffraction and scattering in the propagation medium. A number of such channel models have been developed based on the classical spatial channel modelling approaches for unpolarized systems (see e.g., [5], [6] and the references therein). Polarized channel models have also been defined within 3GPP [7], WINNER [8], and COST [9]. These models are predominantly based on the spatial channel modelling approach without account for recursive scattering.

Motivated by the need to study the effects of recursive and non-recursive scattering on wireless channel characterization, an alternative modelling framework based on directed propagation graph have been presented in [10]–[12]. The graph based model describes the propagation channel as a directed graph with the transmitters, receivers and scatterers as vertices and interactions between vertices defined as a time-invariant transfer function. Based on the graph description, closed-form expressions for the channel transfer function is given in [12]. The graph may be generated using deterministic, stochastic or a combination of determistic and stochastic approach as done in the example model in [12]. Modelling the channel using a propagation graph offers a number of benefits over classical ray-tracing or geometry based spatial channel modelling. Graph based modelling also allows analytical computation of the channel transfer function based on the concept of electromagnetic wave reverberation. Graph based models have relatively low computational complexity when compared to other modelling methods and are straightforward to generalize to multi-user MIMO and different frequency bands. Another important feature of the graph model is the ability to capture via its recursive structure, the avalanche effects and diffuse components with only specular components.

Several other studies have recently presented applications and/or modifications of the graph based models to various propagation environments such as indoor [13], [14], multi-room [15], [16], indoor-to-outdoor [17], high speed railway [18]–[21] and millimeter wave systems [22]. Hybrid models combining the propagation graph based model with ray tracing approaches have also been studied in [23]–[26]. To the best of our knowledge, there has been no study on propagation graph modelling for polarized channels.

In this paper, we extend the propagation graph model [12] to wireless channels with polarized antenna and derive expres-

Ramoni Adeogun and Troels Pedersen are with the Wireless Communication Networks Section, Department of Electronics Systems, Aalborg University, Denmark. E-mail: [ra,troels]@es.aau.dk

Carl Gustafson is with SAAB Dynamics, Linköping, Sweden. E-mail: carl.gustafson@saabgroup

Fredrik Tufvesson is with the Department of Electrical and Information Technology, Lund University, Sweden. E-mail: fredrik.tufvesson@eit.lth.se

sions for the transfer functions. Modelling changes in the polarization state of a propagating wave is an important feature of models for polarized wireless channels. Signal depolarization and cross-polarization coupling in wireless channels are due to three major mechanisms viz: antenna cross-polar isolation (XPI), array mismatch, and interaction of electromagnetic waves with scatterers [27], [28].

We assume that the depolarization effect due to antenna XPI is incorporated into the array response. This is reasonable since XPI is an antenna effect. Depolarization due to array mismatch can be represented as a rotation around an appropriately chosen axis [29]. We therefore assume that depolarization due to array mismatch is incorporated into the polarimetric array responses. Thus, we incorporate polarization dependent propagation characteristics including depolarization, polarization power coupling and antenna polarimetric response into the model. This generalization has been partly presented in a previous work [30].

We derive approximate expressions for predicting the co- and cross-polar power, cross-polarization ratio (XPR) and kurtosis of the output of a propagation graph. The expressions relate these important statistics of any polarized channel to model parameters for the propagation graph (i.e., number of scatterers, probability of visibility, polarization coupling parameter and reflection gain). The expressions may also be used for evaluating averaged statistics of the channel without performing Monte Carlo simulations using the model. The basis for deriving approximate models for polarimetric power delay profile has been partly presented in [31].

We further developed a method of moment based procedure for calibrating the model using channel measurements. The procedure involve fitting estimates of channel statistics to equivalent approximate expressions. Finally, we perform Monte Carlo simulations to verify the closed form approximations, evaluate the performance of the model calibration procedure, and validate the proposed model using dual polarized channel measurements at $60\,\mathrm{GHz}$ and $15\,\mathrm{GHz}$.

## II. Polarized Propagation Graphs

In this section, we extend the propagation graph based modeling framework in [12] to polarized wireless channels. Hence, we consider a simple directed graph $\mathcal{G} = (\mathcal{V}, \mathcal{E})$ with vertex set $\mathcal{V} = \mathcal{V}_\mathrm{t} \cup \mathcal{V}_\mathrm{s} \cup \mathcal{V}_\mathrm{r}$ which is a union of three disjoint sets: a set of $N_\mathrm{t}$ transmitters, $\mathcal{V}_\mathrm{t}$, a set of $N_\mathrm{s}$ scatterers, $\mathcal{V}_\mathrm{s}$ and a set of $N_\mathrm{r}$ receivers, $\mathcal{V}_\mathrm{r}$. Wave propagation between the vertices is modelled by edges in $\mathcal{E} = \mathcal{E}_\mathrm{d} \cup \mathcal{E}_\mathrm{t} \cup \mathcal{E}_\mathrm{s} \cup \mathcal{E}_\mathrm{r}$, where $\mathcal{E}_\mathrm{d}$ is a set of direct edges, $\mathcal{E}_\mathrm{t}$ is a set of transmitter to scatterer edges, $\mathcal{E}_\mathrm{s}$ is a set of scatterer to scatterer edges and $\mathcal{E}_\mathrm{r}$ is a set of scatterer to receiver edges. An edge, $e = (v, w)$, exists if and only if a wave can propagate directly from $v$ to $w$. The propagation graph exhibits a special structure; transmit vertices have no incoming edges; receive vertices have no outgoing edges; and there are no loops in the graph, i.e., no edge, $e = (w, w)$ is possible between the same vertex, $w$. It should however be noted that cycles may exist in the graph.

To describe polarized wave propagation, we introduce a global coordinate system where the vertical ($z$-axis) corresponds to the zenith and the horizontal axes ($x$- and $y$-axis) are parallel to the ground.

Wave propagation in the graph is defined by the actions of the vertices and edges. For a vertex, we define a state vector which denotes the signal emitted by the vertex. For a transmitter, this is the scalar transmitted signal, $\mathbf{X}_v(f), v \in \mathcal{V}_\mathrm{t}$. Similarly, for a receiver, $v \in \mathcal{V}_\mathrm{r}$, the state vector is the scalar received signal, $Y_v(f)$. For a scatterer, $v \in \mathcal{V}_\mathrm{s}$, the state $Z_v(f)$ is the vector defining the signal emitted by the scatterer in all polarization states. Assuming that the waves impinging upon all vertices plane, the signal emitted at a scatterer is a linear combination of the signals arriving via the incoming edges.

Edges transfer the signal between vertices. To edge, $e$ is associated a propagation direction defined by a unit vector $\Omega_e$ which can be represented in polar coordinates as angles $\phi_e$ and $\theta_e$ in the azimuth and co-elevation, respectively. With reference to $\Omega_e$, the signal (representing a transverse electromagnetic wave) propagating along edge, $e$ can be decomposed into $\theta$- and $\phi$-polarized components. Let $e = (v, w)$ and $Z_v(f)$ denote the signal emitted into the edge by $v$, the output signal, $Z_w^{(e)}(f)$, can be expressed as:

$$Z_w^{(e)}(f) = \mathbf{A}_e(f, \Omega_e) Z_v(f) \tag{1}$$

where $\mathbf{A}_e(f, \Omega_e)$ is the polarimetric edge transfer function which is either a scalar for $e \in \mathcal{E}_\mathrm{d}$, $1 \times 2$ vector for $e \in \mathcal{E}_\mathrm{t}$, a $2 \times 2$ matrix for $e \in \mathcal{E}_\mathrm{s}$ or a $2 \times 1$ vector for $e \in \mathcal{E}_\mathrm{r}$. The polarimetric edge transfer matrix incorporates the antenna effect (if either vertex on the edge is a transmitter or receiver), the distance dependent propagation effect and polarization coupling due to interaction with a scatterer and can be represented as

$$\mathbf{A}_e(f, \Omega_e) = \begin{cases} \mathcal{X}_\mathrm{t}^T(\Omega_e) \mathcal{X}_\mathrm{r}(\Omega_e) G_e(f); & e \in \mathcal{E}_\mathrm{d} \\ \mathcal{X}_\mathrm{t}^T(\Omega_e) \mathbf{M}_w(f) \mathbf{\Gamma}(\Omega_e) G_e(f); & e \in \mathcal{E}_\mathrm{t} \\ \mathbf{M}_w(f) \mathbf{\Gamma}(\Omega_e) G_e(f); & e \in \mathcal{E}_\mathrm{s} \\ \mathcal{X}_\mathrm{r}(\Omega_e) G_e(f); & e \in \mathcal{E}_\mathrm{r} \\ \mathbf{0}; & e \notin \mathcal{E}, \end{cases} \tag{2}$$

where $\mathcal{X}_\mathrm{t}(\mathbf{\Omega}_e)$ and $\mathcal{X}_\mathrm{r}(\mathbf{\Omega}_e)$ are the $2 \times 1$ transmit and receive polarimetric array response vectors, respectively. The $2 \times 2$ matrix $\mathbf{\Gamma}(\Omega_e)$ rotates the polarization states of a signal propagating on the edge with direction $\mathbf{\Omega}_e$ such that its direction is aligned with the $z$-axis of the global coordinates. The scalar $G_e(f)$ captures the polarization-independent propagation characteristics (i.e., attenuation, delay spread and phase shift) on the edge. Coupling between the two polarization states is represented by the $2 \times 2$ scattering matrix $\mathbf{M}(f)$ defined as

$$\mathbf{M}_w(f) = \begin{bmatrix} m_{\theta\theta}(f) & m_{\theta\phi}(f) \\ m_{\phi\theta}(f) & m_{\phi\phi}(f) \end{bmatrix}, \tag{3}$$

where $m_{ab}(f)$ denotes power coupling between polarization states $a$ and $b$.

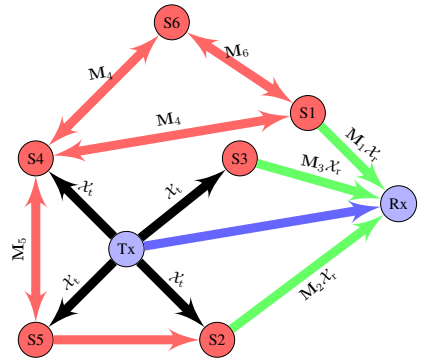


Fig. 1: Example of a propagation graph for a polarized channel with one transmitter, one receiver and six scatterers. Blue arrow represents the direct edges from transmitter to receiver. Black(green) and red arrows denote the transmitter(receiver) to scatterer and inter-scatterer edges, respectively.

Combining (1) with the action of a vertex, the signal at the output of vertex, $w$ in the graph has the form:

$$Z_w(f) = \begin{cases} X_w(f); & w \in \mathcal{V}_\mathrm{t} \\ Y_w(f); & w \in \mathcal{V}_\mathrm{r} \\ \sum_{v\in\mathcal{V}} \mathbf{A}_e(f,\Omega_e) Z_v(f); & w \in \mathcal{V}_\mathrm{s}. \end{cases} \tag{4}$$

Propagation in the polarized graph can be described by a $(N_\mathrm{t}+N_\mathrm{r}+2N_\mathrm{s})\times(N_\mathrm{t}+N_\mathrm{r}+2N_\mathrm{s})$ polarimetric weighted adjacency matrix, $\mathbf{A}(f)$ whose entries are the polarized edge transfer function. $\mathbf{A}(f)$ is of the form,

$$\mathbf{A}(f) = \begin{bmatrix} \mathbf{0} & \mathbf{0} & \mathbf{0} \\ \mathbf{D}(f) & \mathbf{0} & \mathbf{R}(f) \\ \mathbf{T}(f) & \mathbf{0} & \mathbf{B}(f) \end{bmatrix}, \tag{5}$$

with sub-matrices:

$$\begin{aligned} \mathbf{D}(f) &\in \mathbb{C}^{N_\mathrm{r}\times N_\mathrm{t}} : \text{transmitters} \to \text{receivers} \\ \mathbf{T}(f) &\in \mathbb{C}^{2N_\mathrm{s}\times N_\mathrm{t}} : \text{transmitters} \to \text{scatterers} \\ \mathbf{R}(f) &\in \mathbb{C}^{N_\mathrm{r}\times 2N_\mathrm{s}} : \text{scatterers} \to \text{receivers} \\ \mathbf{B}(f) &\in \mathbb{C}^{2N_\mathrm{s}\times 2N_\mathrm{s}} : \text{scatterers} \to \text{scatterers}. \end{aligned} \tag{6}$$

It should be noted that although the polarimetric adjacency matrix has the same structure as given in [12] for the uni-polarized channel, the dimension and structure of the polarized sub-matrices differs from those in [12]. Assuming that the channel is time-invariant, the received signal vector $\mathbf{Y}(f)$ reads

$$\mathbf{Y}(f) = \mathbf{H}(f)\mathbf{X}(f), \tag{7}$$

where $\mathbf{X}(f)$ is the transmitted signal vector and $\mathbf{H}(f)$ is the polarized transfer matrix. Following a similar procedure as in [12], $\mathbf{H}(f)$ of the propagation graph is obtained as

$$\mathbf{H}(f) = \mathbf{D}(f) + \mathbf{R}(f)[\mathbf{I} - \mathbf{B}(f)]^{-1}\mathbf{T}(f), \tag{8}$$

provided that the spectral radius of $\mathbf{B}(f)$ is less than unity.

## III. Stochastic Polarized Channel Model

The polarized propagation graph described in Section II is valid for general edge transfer functions and scattering matrices. Therefore, to compute channel transfer matrices from (8), it is necessary to specify the scattering matrix, $\mathbf{M}_w(f)$ and edge transfer functions, $\mathbf{A}_e(f)$. An example of how to define the edge transfer functions of a propagation graph for an in-room scenario assuming only specular reflections is given in [12]. We define the polarization independent component of the polarimetric edge transfer function based on this example model and highlight the procedure for stochastic generation of the polarized channel in this section.

### A. Models for Gains and Polarimetric Scattering Matrix

As in [12], the polarization-independent transfer function of the edge, $e$ can be expressed as

$$G_e(f) = g_e(f)\exp[j(\psi_e - 2\pi\tau_e f)], \tag{9}$$

where $\psi_e$ and $\tau_e$ denote the phase and propagation delay, respectively. The edge propagation delay can be calculated for edge, $e = (v_n, v_m)$ from the vertex position vectors, $\mathbf{r}_{n/m}$ as $\tau_e = |(\mathbf{r}_m - \mathbf{r}_n)|/c$, where $c$ is the speed of light and $||$ denotes norm of the associated vector. The edge gain, $g_e(f)$ can be calculated from [12]

$$g_e(f) = \begin{cases} \frac{1}{(4\pi f\tau_e)}; & e \in \mathcal{E}_\mathrm{d} \\ \frac{1}{\sqrt{4\pi\tau_e^2 f\mu(\mathcal{E}_\mathrm{t})\mathcal{S}(\mathcal{E}_\mathrm{t})}}; & e \in \mathcal{E}_\mathrm{t} \\ \frac{g}{\mathrm{odi}(e)}; & e \in \mathcal{E}_\mathrm{s} \\ \frac{1}{\sqrt{4\pi\tau_e^2 f\mu(\mathcal{E}_\mathrm{r})\mathcal{S}(\mathcal{E}_\mathrm{r})}}; & e \in \mathcal{E}_\mathrm{r}, \end{cases} \tag{10}$$

Here, $g$ denotes the reflection gain, $\mathrm{odi}(e)$ denotes the number of outgoing edges from the $n$th scatterer,

$$\mu(\mathcal{E}_\mathrm{a}) = \frac{1}{|\mathcal{E}_\mathrm{a}|}\sum_{e\subset\mathcal{E}_\mathrm{a}} \tau_e, \quad \mathcal{S}(\mathcal{E}_\mathrm{a}) = \sum_{e\subset\mathcal{E}_\mathrm{a}} \tau_e^{-2}, \quad \mathcal{E}_\mathrm{a} \subset \mathcal{E}, \tag{11}$$

where $|\cdot|$ denotes set cardinality.

We assume for simplicity that the scattering matrix is equal for all scatterers and model the polarization transfer matrix at each scatterer as

$$\mathbf{M} = \frac{1}{1+\gamma}\begin{bmatrix} 1 & \gamma \\ \gamma & 1 \end{bmatrix}, \tag{12}$$

where $\gamma$ is the polarization power coupling parameter and ranges from 0 to 1.

### B. Stochastic Generation of Polarized Channels

We assume that the position of all vertices lie in a bounded region, representing the part of the propagation environment affecting the received signal. The transmitter and receiver locations are assumed to be fixed and known whereas scatterer positions are drawn randomly according to a specified spatial scatterer distribution over the bounded region. The transmitter

Algorithm 1: Stochastic Generation of Polarized Channel

**Input:** Model parameters: $N_{\rm s}, P_{\rm vis}, g, \gamma,\ f_{\min}, f_{\max}, \Delta f$ and room dimensions.

1: Specify the coordinates of the transmitter(s) and receiver(s).
2: Draw the positions, $\mathbf{r}_n$ of $N$ scatterers according to the specified spatial scatterer distribution.
3: Generate edges independently according to the edge occurrence probability in (13).
4: Compute edge gains using (9) and polarimetric edge transfer functions using (2).
5: Compute $\mathbf{H}(f);\quad f = f_{\min}, f_{\min}+\Delta f, \cdots, f_{\max}$ using (8)
6: Compute channel impulse response, $h(\tau)$ via inverse discrete Fourier transform.

**Output:** $\mathbf{H}(f);\quad \mathbf{h}(\tau)$

and receiver positions may also be drawn randomly, if desired. An edge $e \in \mathcal{E}$ is drawn with probability

$$\Pr[e \in \mathcal{E}] = \begin{cases} P_{\rm dir}, & e \in \mathcal{E}_{\rm d} \\ P_{\rm vis}, & e \in (\mathcal{E}_{\rm t}, \mathcal{E}_{\rm s}, \mathcal{E}_{\rm r}) \\ 0, & \text{otherwise.} \end{cases} \tag{13}$$

The phases $\psi_e$ are drawn independently from a uniform distribution on $[0, 2\pi)$ and edge gains are computed using (5). We specify a value for the polarization coupling parameter, $\gamma$ and compute the scattering matrix using (12). Based on these parameters of the graph, entries of the graph adjacency matrix are computed using (2). The polarized channel transfer function is computed over the desired frequency range, $[f_{\min}, f_{\max}]$ from (8). The time domain channel impulse response of the polarized channel is then obtained via a windowed inverse Fourier transform of the transfer function. The polarized channel generation procedure is summarized in Algorithm. 1.

## IV. Analysis of the Polarimetric Power Delay Spectrum

We analyze the polarimetric power delay spectrum (PDS)[1] by using an approximation and validate this approximation via simulations. We approximate the full propagation graph by a simpler graph as shown in Fig. 2.

We consider the transmitted signal as a power pulse emitted at time, $\tau = 0$, i.e., $P_{\rm t} = |\mathbf{X}|^2$. For simplicity, we assume that $\mathbf{X}(\tau) = \delta(\tau)$. Ignoring the direct component, the power of the received signal at time $\tau$ is expressed as

$$P_{\rm r}(\tau) = \mathcal{G}_{\rm r}^T P_{\rm s}(\tau) \mathcal{G}_{\rm t}. \tag{14}$$

[1]The power delay spectrum (PDS) is used here to denote expectation of the power delay profile (PDP) considering the limiting case of infinite bandwidths [32], [33]. For simulated channels, the PDS is approximated by the averaged power delay profile (APDP) obtained for a high (but finite) bandwidth signal.

Here, the vectors, $\mathcal{G}_{\rm r/t}$ denote the receiver/transmitter polarimetric array response vector averaged over all directions and are defined as

$$\begin{aligned} \mathcal{G}_{\rm t/r} &= [\mu^{\theta}_{\rm t/r} \quad \mu^{\phi}_{\rm t/r}]^T \\ &= \frac{1}{4\pi} \int_0^{2\pi} \int_0^{\pi} \mathcal{X}_{\rm t/r}(\theta, \phi) \sin\theta d\theta d\phi, \end{aligned} \tag{15}$$

where $\mu^{\theta}_{\rm t/r}$ and $\mu^{\phi}_{\rm t/r}$ denote the $\theta$- and $\phi$-polarized component of the averaged transmit/receive antenna response, respectively.

The power of the scattered component, $P_{\rm s}(\tau)$ is approximated as follows. First, we consider the mean time between scattering interactions, $\mu_\tau$. This we equate to the ratio of the mean cord length of the room and speed of light, which is [32], [34],

$$\mu_\tau = \frac{4V}{cS}, \tag{16}$$

where $V$ and $S$ are the volume and total surface area of the room, respectively.

Consider the power received from paths arriving after $k$-bounces, $P_{\rm s}[k]$ which can be cast as

$$P_{\rm s}[k] = \Upsilon \mathbb{E}[N_k] \mathbb{E}[U_k], \tag{17}$$

where $N_k$ and $U_k$ denote the number of $k$-bounce paths and the power per $k$-bounce path, respectively. The scaling factor, $\Upsilon$, accounts for the power decay during the average period associated with the transmitter to scatterer and scatterer to receiver edges. Approximating the time per edge by $\mu_\tau$, $\Upsilon$ is obtained from (10) as

$$\Upsilon = \left(\frac{1}{4\pi f \mu_\tau}\right)^2. \tag{18}$$

To obtain an approximation for $P_{\rm s}[k]$, we shall approximate the last two factors. With high $P_{\rm vis}$, the second factor is well approximated as

$$\mathbb{E}[N_k] \approx P_{\rm vis} N_s (P_{\rm vis}(N_s - 1))^{k-1}. \tag{19}$$

The third factor is approximately,

$$\mathbb{E}[U_k] \approx \frac{(g^2)^{k-1} M^k}{P_{\rm vis} N_s (P_{\rm vis}(N_s-1))^k}, \tag{20}$$

Substituting (19) and (20) into (17) yields

$$P_{\rm s}[k] = \frac{\Upsilon (g^2)^{k-1} M^k}{P_{\rm vis}(N_s - 1)} \tag{21}$$

The expression in (21) gives the average power level of paths arriving after $k$ bounces. We assume that all k-bounce paths, will on average arrive with excess delay $\tau = (k-1)\mu_\tau$ relative to the time delay of a 1-bounce path. The number of bounce index $k$ can therefore be replaced with $\tau/\mu_\tau + 1$ yielding a discrete function $P_{\rm s}[\tau];\quad \tau = 0, \mu_\tau, 2\mu_\tau, \cdots$. Relaxing to any real $\tau$, we obtain

$$P_{\rm s}(\tau) = \frac{\Upsilon g^{(2\tau/\mu_\tau)} \mathbf{M}^{(1+\tau/\mu_\tau)}}{P_{\rm vis}(N_{\rm s} - 1)}. \tag{22}$$

Substituting (22) into (14) yields

$$P_{\rm r}(\tau) = \mathcal{G}_{\rm r}^T \frac{\Upsilon g^{(2\tau/\mu_\tau)} \mathbf{M}^{(1+\tau/\mu_\tau)}}{P_{\rm vis}(N_{\rm s} - 1)} \mathcal{G}_{\rm t}. \tag{23}$$

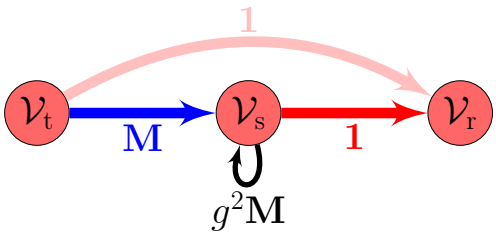


Fig. 2: Simplified model for the power transfer in a graph. Labels on the edges represent power gain without delay dependent decay and antenna responses.

Inserting the eigenvalue decomposition of $\mathbf{M}$ and using (15) yields after some simplifications,

$$P_\mathrm{r}(\tau) = \frac{\Upsilon g^{(2\tau/\mu_\tau)}(\mu_\mathrm{t}^\theta \mu_\mathrm{r}^\theta + \mu_\mathrm{t}^\phi \mu_\mathrm{r}^\phi)}{2P_\mathrm{vis}(N_\mathrm{s}-1)} \left\{1 + \left(\frac{1-\gamma}{1+\gamma}\right)^{(1+\tau/\mu_\tau)}\right\} + \frac{\Upsilon g^{(2\tau/\mu_\tau)}(\mu_\mathrm{t}^\theta \mu_\mathrm{r}^\phi + \mu_\mathrm{t}^\phi \mu_\mathrm{r}^\theta)}{2P_\mathrm{vis}(N_\mathrm{s}-1)} \left\{1 - \left(\frac{1-\gamma}{1+\gamma}\right)^{(1+\tau/\mu_\tau)}\right\}. \tag{24}$$

The first and second terms of (24) are the co- and cross-polar components of the PDS, respectively. It appears that the decay of the PDS is controlled by the average reflection gain, $g$ and polarization mixing parameter, $\gamma$. However, the effect of $\gamma$ vanishes with increasing delay. The expression in (24) is valid for general polarimetric antenna responses. Special cases appear by inserting values for $\mu_{\mathrm{t/r}}^{\theta/\phi}$.

### *A. Special Case:Lossless Antennas With Perfect Cross-Polar Isolation*

For a lossless antenna, the principle of conservation of energy implies that $\mu_{\mathrm{t/r}}^\theta + \mu_{\mathrm{t/r}}^\phi = 1$. Furthermore, with perfect cross-polar isolation, the co- and cross-polar averaged responses become one and zero, respectively.

With $\mathcal{G}_\mathrm{t} = [1 \quad 0]^T$ and $\mathcal{G}_\mathrm{r} = [1 \quad 0]^T$, (24) gives the co-polar PDS as

$$P_\mathrm{co}(\tau) = \frac{\Upsilon g^{(2\tau/\mu_\tau)}}{2P_\mathrm{vis}(N_\mathrm{s}-1)} \left\{1 + \left(\frac{1-\gamma}{1+\gamma}\right)^{(1+\tau/\mu_\tau)}\right\}. \tag{25}$$

The cross-polar PDS obtained with $\mathcal{G}_\mathrm{t} = [1 \quad 0]^T$ and $\mathcal{G}_\mathrm{r} = [0 \quad 1]^T$ is

$$P_\mathrm{cro}(\tau) = \frac{\Upsilon g^{(2\tau/\mu_\tau)}}{2P_\mathrm{vis}(N_\mathrm{s}-1)} \left\{1 - \left(\frac{1-\gamma}{1+\gamma}\right)^{(1+\tau/\mu_\tau)}\right\}. \tag{26}$$

In the region where $\tau \gg \mu_\tau$ (i.e., tail of the PDS), the co- and cross-polar PDS decay exponentially as

$$P_\mathrm{co/cro}(\tau) \approx \frac{\Upsilon g^{(2\tau/\mu_\tau)}}{2P_\mathrm{vis}(N_\mathrm{s}-1)}, \tag{27}$$

The polarimetric PDS in (27) is independent of the polarization coupling parameter $\gamma$ and shows that in the later part of the profile, the co- and cross-polar channels become approximately equal both in power level and decay rate. Based on (27), the decay rate of the PDS is then defined as

$$\rho \approx \frac{20}{\mu_\tau}\log_{10}(g) \quad [\mathrm{dB/s}]. \tag{28}$$

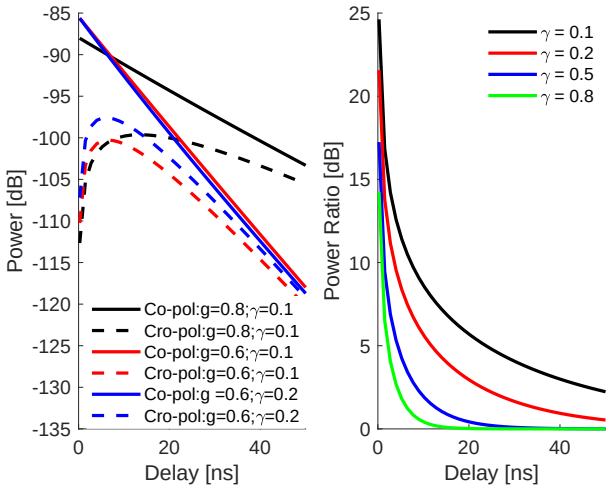


Fig. 3: Dependence of channel statistics on model parameters for a $3 \times 4 \times 3\,\mathrm{m}^3$ room. The LOS term is set to zero.

Thus, $\rho$ is controlled by the average reflection gain, $g$ and the mean interaction delay, $\mu_\tau$.

The cross-polar power ratio, denoted here as $\beta$ is obtained from (25) and (26) as

$$\beta(\tau) = \frac{P_\mathrm{co}(\tau)}{P_\mathrm{cro}(\tau)} = \frac{1 + \left(\frac{1-\gamma}{1+\gamma}\right)^{(1+\tau/\mu_\tau)}}{1 - \left(\frac{1-\gamma}{1+\gamma}\right)^{(1+\tau/\mu_\tau)}}. \tag{29}$$

For $\tau \gg \mu_\tau$, (29) becomes one.Fig. 3 shows an example of the approximate power delay spectrum and cross-polarization ratio with different model parameters. As predicted by (27), the co- and cross-polar power delay spectra approach each other with increasing delay and become nearly equal.

## V. Model Calibration

To utilize the proposed model, specific values should be given to the parameters, $\boldsymbol{\Theta} = [g, N_s, P_{vis}, \gamma]$. Here, we calibrate the model by estimating these parameters from measurements of the channel transfer function. To this end, we derive a method of moment (MoM) [35] based estimator for the model parameters. We estimate the parameters by fitting estimated moments of the measured channel to the expressions derived in in Section IV.

### *A. MoM Based Model Calibration Procedure*

To calibrate the model, we fit estimates of the second moments of PDS and cross-polarization ratio to the expressions (25), (26) and (29). Since $N_\mathrm{s}$ and $P_\mathrm{vis}$ are not identifiable in the PDS and cross-polarization ratio, we therefore introduced the product $\nu = (N_\mathrm{s}-1)P_\mathrm{vis}$ as a parameter. This identifiability problem can be overcome by selecting a value for either parameter and computing the other from the estimate of the product, $\nu$. While it is advantageous for computational complexity reasons to select a low value for $N_\mathrm{s}$, choosing a

reasonable value to reproduce the scattering in a particular environment may be difficult. We therefore, propose setting value of $P_{\text{vis}}$ in this paper. It is relatively straightforward to set values of $P_{\text{vis}}$ since probability values are bounded (i.e., $0 < P_{\text{vis}} \leq 1$) and relates intuitively to the density of objects in the room. Note that further work may be needed on characterizing the probability of visibility and determining these values for different types of propagation environment.

Given the measured channel transfer matrices $\mathbf{H}(f); f \in [f_{\min} \quad f_{\max}]$, we compute the impulse response $h(\tau)$; for all polarizations and estimate the model parameters following the calibration procedure in Algorithm 2.

Algorithm 2: MoM Based Model Calibration Procedure

**Input:** Measured impulse response; $h(\tau); \tau = \tau_{\min} \ldots \tau_{\max}$ for co- and cross-polar channels and $P_{\text{vis}}$.

1: Compute the PDS, $\hat{\mathbf{P}}_{\text{co}}$ and $\hat{\mathbf{P}}_{\text{cro}}$ and cross-polarization ratio, $\hat{\boldsymbol{\beta}}$ from $\mathbf{h}(\tau)$.[2].
2: Estimate the decay rate, $\rho$ from the slope of $\hat{\mathbf{P}}_{\text{co}}$ and solve (28) for $\hat{g}$.
3: Estimate the polarization mixing parameter, $\hat{\gamma}$ by fitting $\hat{\boldsymbol{\beta}}$ to (29).
4: Find $\hat{\nu}$ by least squares fitting of the sum of (25) and (26) to $\hat{\mathbf{P}}_{\text{co}} + \hat{\mathbf{P}}_{\text{cro}}$.
5: Compute $\hat{N}_{\text{s}} = \hat{\nu}/P_{\text{vis}}$

**Output:** Model parameters: $\hat{\boldsymbol{\Theta}} = [\hat{g}, \hat{N}_s, P_{vis}, \hat{\gamma}]$

### *B. Verification of Approximate Polarimetric Power Delay Spectrum*

We compare predictions of the power delay profile and cross-polarization ratios from the approximate expressions to those obtained from the graph model. We consider two scenarios in the evaluation:

- *Graph Model I*: Transmitter and receiver locations are fixed and equal for each realization of the propagation graph, and
- *Graph Model II*: Transmitter and receiver locations are random and drawn uniformly within the room for each channel realization.

Fig. 4 reports estimated PDS and XPR obtained by averaging power delay profiles over 1000 Monte Carlo runs with the settings in Table II. The approximate PDS shows very good agreement with the simulated PDS from the model for the two scenarios. The XPR plots also show that the predicted and simulated cross-polarization delay profile exhibits very good agreement with a difference less than $1\,\text{dB}$ over the entire delay values shown.

### *C. Model Calibration Performance*

In order to evaluate the performance of the proposed calibration procedure, we first test the method on simulated data before applying the procedure on the measured data sets. We consider an in-room scenario with parameters in Table II and different combinations of the model parameters. The number of estimates of the PDS utilized in the calibration is set to

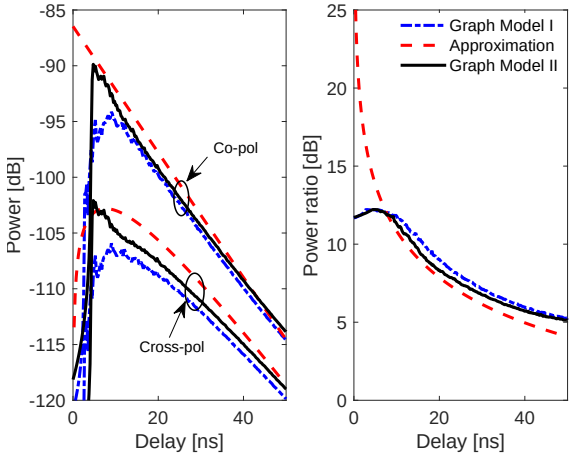


Fig. 4: Simulated power delay profile and cross-polarization ratio from the propagation graph and approximate expressions.

TABLE I: Performance of model calibration procedure evaluated via simulation with fixed transmitter and receiver positions.

| | $g$ | $\gamma$ | $\nu$ | $P_{\text{vis}}$ | $N_{\text{s}}$ |
|---|---|---|---|---|---|
| True | 0.70 | 0.20 | 12.60 | 0.90 | 15 |
| Estimate | 0.72 | 0.20 | 12.46 | 0.90 | 15 |
| % Error | 2.86 | 0.90 | 1.12 | – | 0 |
| True | 0.80 | 0.10 | 8.80 | 0.70 | 12 |
| Estimate | 0.80 | 0.10 | 8.62 | 0.70 | 12 |
| % Error | 0.14 | 2.06 | 0.95 | – | 0 |
| True | 0.60 | 0.40 | 7.20 | 0.80 | 10 |
| Estimate | 0.61 | 0.39 | 7.11 | 0.80 | 10 |
| % Error | 1.67 | 2.50 | 1.13 | – | 0 |
| True | 0.65 | 0.05 | 17.48 | 0.92 | 20 |
| Estimate | 0.65 | 0.05 | 17.20 | 0.92 | 20 |
| % Error | 0.17 | 0 | 1.60 | – | 0 |

$K = 200$ with $\tau_1 = 7.75\,\text{ns}$ and $\tau_K = 57.75\,\text{ns}$. The true and estimated parameters are presented in Table I. The probability of visibility which is chosen and number of scatterers obtained from $\hat{\nu}$ are included in the table for completeness. As shown in Table I, all model parameters are accurately estimated with calibration error less than $3\,\%$ for all parameter values. Thus, we consider the procedure to be sufficiently accurate to calibrate the model.

## VI. Measurement Datasets

Three measurement datasets named M1, M2, and M3 are used for calibration and validation of the polarized propagation graph model. The three datasets summarized below are obtained from measurement campaigns conducted at Lund University, Sweden, and are reported in [36] and [37].

### *A. 60 GHz Small Room Measurement (M1)*

The dataset M1 was obtained using a VNA at $60\,\text{GHz}$ in a $3 \times 4 \times 3\,\text{m}^3$ meeting room. It is comprised of four LOS and four NLOS datasets. For each measurement location, the transmitter and receiver has a $5 \times 5$ virtual dual polarized rectangular array in the horizontal and vertical plane, respectively. The transmit virtual arrays are obtained by moving the virtual element at a regular interval of $5\,\text{mm}$ along the $y-$ and $z$-axis

TABLE II: Measurement settings for M1, M2 and M3.

| | Measurement | | |
|---|---|---|---|
| | M1 | M2 | M3 |
| Room size | $3 \times 4 \times 3\,\mathrm{m}^3$ | $6 \times 10 \times 3\,\mathrm{m}^3$ | $6 \times 6 \times 3\,\mathrm{m}^3$ |
| Tx height | $2.35\,\mathrm{m}$ | $2.00\,\mathrm{m}$ | $1.00\,\mathrm{m}$ |
| Rx height | $1.85\,\mathrm{m}$ | $2.50\,\mathrm{m}$ | $1.00\,\mathrm{m}$ |
| Freq. range | $58\,\mathrm{GHz} - 62\,\mathrm{GHz}$ | $14.5\,\mathrm{GHz} - 15.5\,\mathrm{GHz}$ | $58\,\mathrm{GHz} - 62\,\mathrm{GHz}$ |
| Num. of freq. samples | 801 | 801 | 801 |

TABLE III: Model parameter estimates obtained from the calibration datasets. $N_\mathrm{s}$ is computed from $\hat{\nu}$ with $P_\mathrm{vis} = 0.90$.

| Meas. | $g$ | $\gamma$ | $N_\mathrm{s}$ |
|---|---|---|---|
| M1 | 0.64 | 0.06 | 11 |
| M2 | 0.65 | 0.26 | 18 |

from the positions shown in Fig. 5a. At the receiver, the virtual element is moved along the $x$- and $y$-axis to form the virtual array. The virtual arrays emulate a $25 \times 25$ dual polarized MIMO system with $50 \times 50$ antenna ports. The height of the transmitter and receiver are $2.35\,\mathrm{m}$ and $1.85\,\mathrm{m}$, respectively. Detailed description of M1 can be found in [36]. The dataset is divided into two groups: M1-cal (NLOS I, NLOS II and LOS I) and M1-val (NLOS IV, LOS II and LOS IV).

### *B.* $15\,\mathrm{GHz}$ *Large Room Measurement (M2)*

The dataset M2 was obtained using a VNA at $15\,\mathrm{GHz}$ in a $6 \times 10 \times 3\,\mathrm{m}^3$ conference room. Measurements were taken using virtual MISO system with a a $10 \times 10$ antenna array at the transmitter and a single monopole at the receiver. The transmitter was placed at a fixed location in the room and the receiver was placed at different locations as shown in 5b. LOS and NLOS measurements from the four receiver locations are used in this work. The height of the transmitter and receiver are $2\,\mathrm{m}$ and $2.5\,\mathrm{m}$, respectively. Detailed description of M2 can be found in [37]. The dataset is grouped into two: M2-cal (LOS I, LOS II , NLOS II and NLOS IV) and M2-val (LOS II, LOS IV , NLOS I and NLOS III).

### *C.* $60\,\mathrm{GHz}$ *Medium Sized Room Measurement (M3)*

The dataset M3 was obtained using a VNA at $60\,\mathrm{GHz}$ in a $6 \times 6 \times 3\,\mathrm{m}^3$ conference room. Measurements were taken using the rotating antenna technique with a high directional horn antenna at the receiver and an omnidirectional biconical antennna at the transmitter. The transmitter and receiver were placed at the locations shown in Fig. 5c with the same height of $1\,\mathrm{m}$. Measurements were taken at every $1^o$ while the receiver is rotated. Detailed description of M3 can be found in [36]. Since M3 and M1 are collected at the same frequency in similar environments, we use M3 for cross validation of the model.

## VII. Model Validation

In this section, we validate the proposed model and approximate expressions using data from the measurements described in section VI. We follow the cross-validation procedure summarized in Fig. 6. We utilized M1-cal and M2-cal for model calibration. With the calibration results from these two datasets, we validate the model using M1-val, M2-val and M3.

The model parameters obtained from the calibration procedure are presented in Table III. Here, we set a high value for the probability of visibility (i.e, $P_\mathrm{vis} = 0.9$)[3] since the measurements were conducted in nearly empty rooms. As can be observed from Fig. 7, the measured PDS and cross-polarization ratio agree closely with the predicted values at the estimated model parameters for both M1-cal and M2-cal.

Fig. 8 shows that the power level and tail decay of the PDS for M1-val are accurately predicted by the model as well as the theoretical approximation. Similar agreements between the validation data, propagation graph and the approximate model are seen in the PDS plots in Fig. 9 for M2-val. We observe in Fig. 8 and Fig. 9 that the measured XPR delay profile exhibit similar trends as the predicted ratios: a transition from a region of decreasing polarization ratio to a region with nearly constant ratio.

We now cross validate the model with M3 data set using estimates obtained from M1. To cross-validate the model, we first estimate these parameters from M1 and then attempt to predict M3. Since these measurements are obtained from rooms with different sizes, we expect that the number of scatterers, $N_\mathrm{s}$, differs. We assume that the number of scatterers is proportional to the total surface area of the room. Thus, with $N_\mathrm{s} = 11$ for M1, $N_\mathrm{s}$ for M3 is set to 24. With these parameters, we observe in Fig. 10 that the power level, decay rate and XPR predictions from the model agree with those obtained from the measurement except for a slight power difference in the cross-polar channel.

The stochastic graph model cannot be expected to represent all features of the measured instantaneous power delay profiles, but as we have seen, to agree well in terms of mean values. Nonetheless, in Fig. 11,we compare single realizations of the model measurements in order to evaluate how well the model represents the behaviour of the instantaneous co- and cross-polar power delay profiles. Three realizations of the propagation graph are shown along with approximation and measured power delay profile for the M1 dataset. As can be observed from Fig. 11, the power level and decay rate of the measured channel are well predicted by the model except for few spikes in the measurements that were not captured by the model. A plausible explanation for this is that these few peaks are due to the presence of very strong reflections from objects in the room which are ignored in the model. We further remark that exact reproduction of the measured profile from the graph model may be possible by using a detailed map and information on the materials of the environment for constructing the propagation graph. This is, however, outside the scope of the present contribution.

## VIII. Discussion

The propagation graph model presented in this paper provides a simple method for simulating the transfer function

[3]With fixed $P_\mathrm{vis}(N_\mathrm{s} - 1)$, $P_\mathrm{vis}$ can be set to lower values without significantly impacting predictions from the model. Our simulations indicate that $P_\mathrm{vis} \geq 0.7$ works well for M1 and M2.

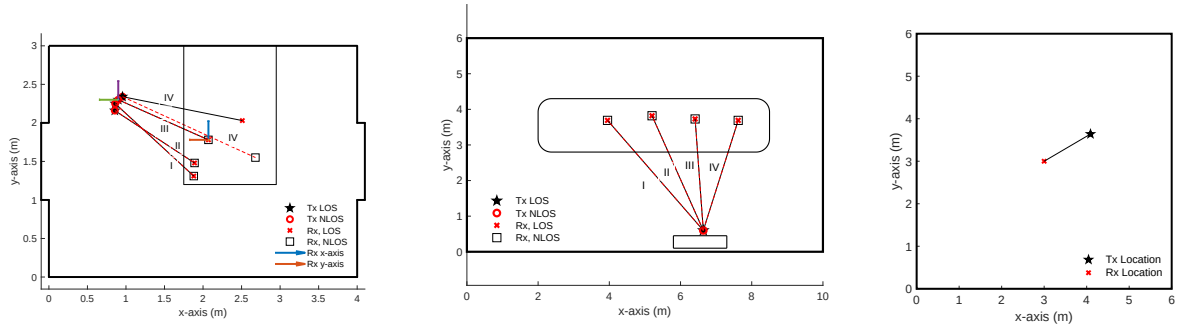


(a) M1. (b) M2 (c) M3

Fig. 5: Floor plan of the measurement setup for M1, M2 and M3.

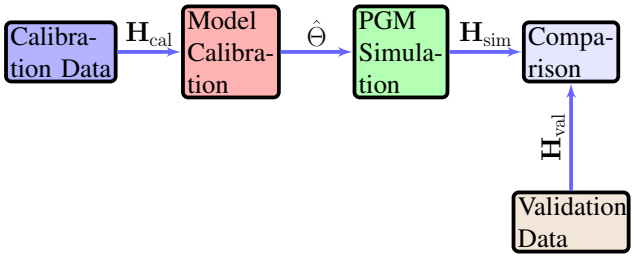


Fig. 6: Model validation procedure. The measurement that is grouped into two - $\mathbf{H}_{\text{cal}}$ and $\mathbf{H}_{\text{val}}$ for model calibration and validation, respectively. $\mathbf{H}_{\text{sim}}$ denotes the simulated channel from realizations of the propagation graph with the model parameters from the calibration stage.

as well as the impulse response of the polarized channel. Stochastic implementation of the model requires only three real valued (reflection gain, probability of visibility and polarization mixing parameter) and one integer valued (number of scatterers) model parameters in addition to basic geometric parameters such as dimensions of the scattering region (i.e., room dimensions for the in-room channel considered in the simulations) and location of transmitter and receiver to accurately predict the polarimetric power delay spectrum of the channel. The model has relatively low complexity in terms of both computational cost and the number of model parameters compared to other models for polarimetric channels. For example, spatial channel models (see e.g., [6], [38]) typically require characterizing parameters of the distribution of a large number of multipath components and/or clusters. It should be noted that the propagation graph model also allows a deterministic approach for generating the channel impulse response. In this case, detailed description of the environment, obtained from a map of the environment and/or an initial ray tracing step may be used to construct adjacency sub-matrices for the propagation graph.

The calibration results for the two measured rooms (M1 and M2) considered showed nearly equal values for the reflection gain. This appears reasonable from a physical point of view, since both rooms are in the same building and most probably made of similar materials. We therefore, expect that regardless of room sizes and transmission frequency, the reflection gain,

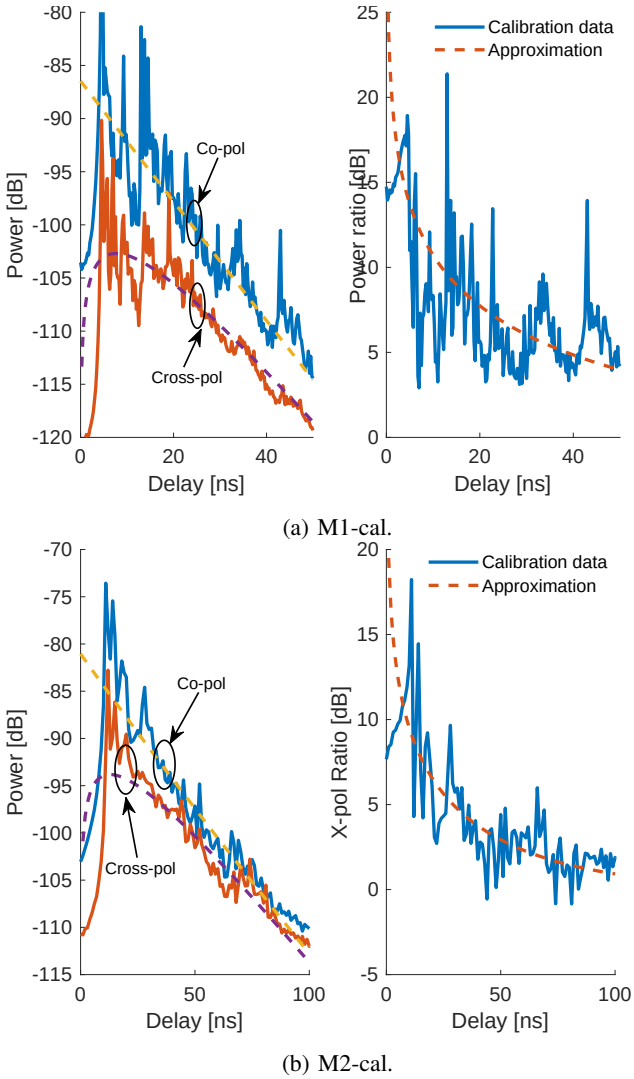


(a) M1-cal.

(b) M2-cal.

Fig. 7: Measured calibration datasets and theoretical PDS and cross-polarization ratio with model parameters in Table III.

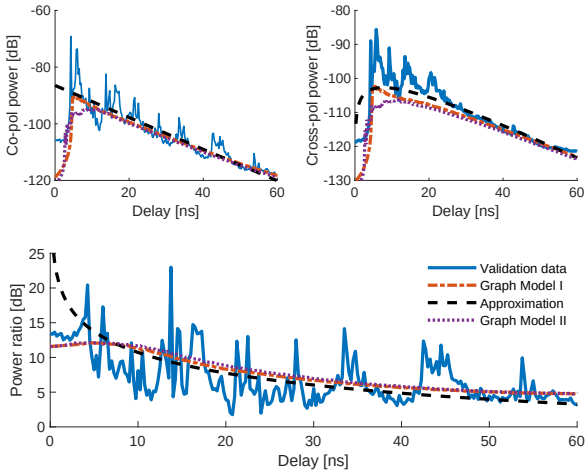


Fig. 8: Measured and averaged simulated polarimetric PDS and XPR for M1-val.

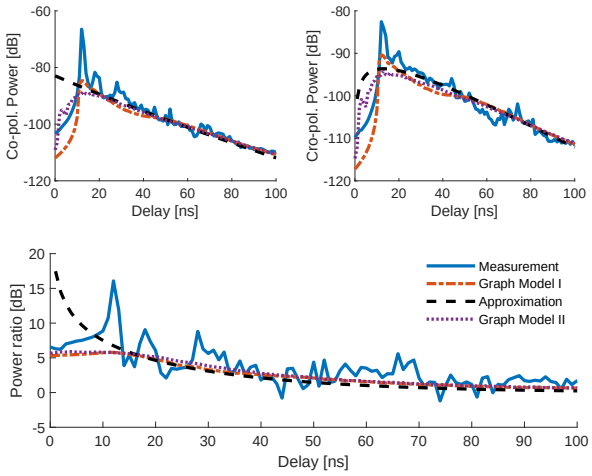


Fig. 9: Measured and averaged simulated polarimetric PDS and XPR for M2-val.

$g$, will be the same for rooms made of similar materials.

With the same value of probability of visibility, estimated number of scatterers is higher for the medium sized room than the small room. This implies that more scatterers are needed to reproduce channel effects in larger rooms. The polarization coupling parameter, $\gamma$ obtained from the calibration is observed to be larger for M2. While this may be due to the increased size and/or difference in frequency, other factors such as polarimetric antenna properties, height and orientation of the antenna may result in significant change in the polarization behaviour of the channel and hence, the coupling parameter. Further study is needed to characterize the dependence of this model parameter on frequency as well as geometrical and environmental effects.

We remark that existing works on polarization sensitive modelling (see e.g., [6], [39] and the references therein) in classical spatial channel modelling literature may provide basis

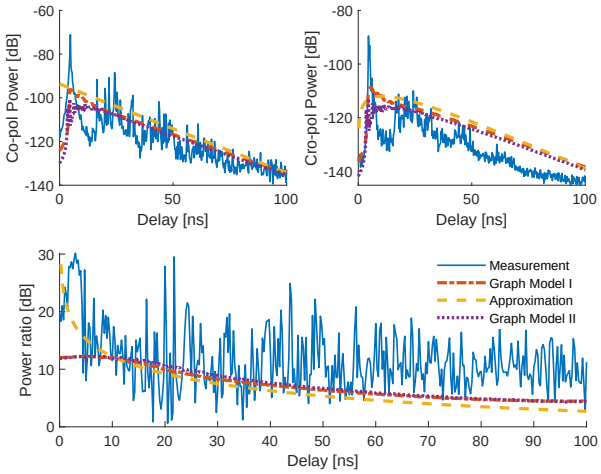


Fig. 10: Measured and averaged simulated polarimetric PDS and XPR for the M3 datasets with model parameters obtained using M1-cal.

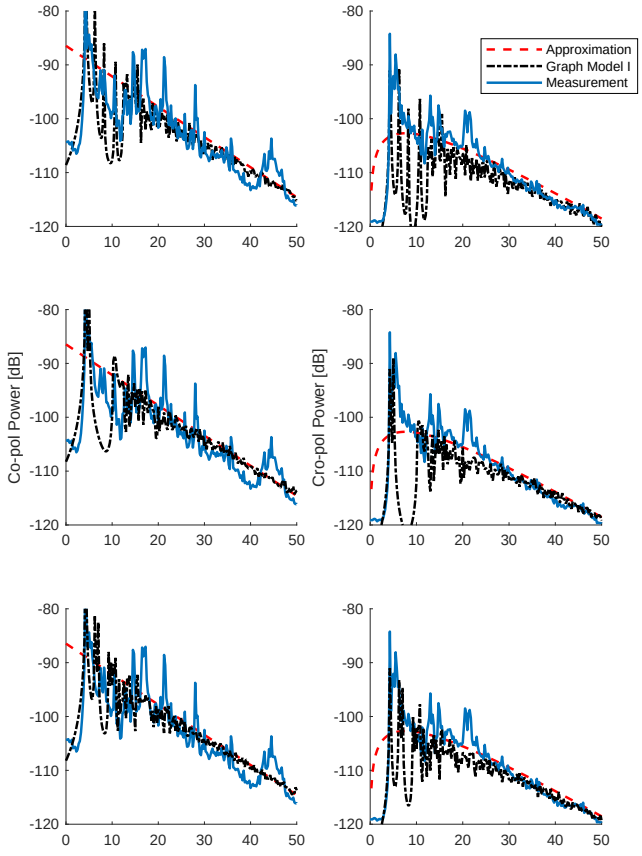


Fig. 11: Realizations of the propagation graph for M1-val.

for characterizing the scatterer polarization coupling parameter and hence, the scattering matrix, $\mathbf{M}$ in terms of propagation and geometry related characteristics. This is however, non-trivial since polarization coupling is represented in these models per path and not on per scatterer basis as required in the propagation graph.

The cross-polar power ratio is observed in measurements and predictions by the model to be decreasing with delay and approaches a constant in the late part of the PDS. Thus, we observe that the model predicts a transition of the propagating signal from a fully polarized state to a partially and/or non-polarized state. This effect is intuitive since power is leaked from one polarization state to an orthogonal state during interaction with scatterers and hence, the ratio between the co- and cross-polar channels decreases with increasing number of interactions.

Although there has been very limited studies on the dependence of XPR on delay in recent times, similar observations have been reported in [40], [41]. While analyzing polarimetric channel measurements at $1800\,\mathrm{MHz}$ in [40], the authors observed that the ratio of co- and cross-polarized channels varies over time. Similarly, it was found in [41] that the co- and cross-polar channels exhibit different decay constants. However, the cross-polarization ratio was shown to increase with delay for the macrocellular environment considered. This contrasting observation was noted in [6] as surprising. For the same macrocellular environment, the cross-polarization ratio is modelled as a decreasing function of delay in the 3GPP model [7]. In a recent study based on measurements at $63\,\mathrm{GHz}$, the cross-polarization ratio is found to decrease with increasing excess loss of the propagation paths [42]. This agree with our observation that the ratio decreases with delay, since propagation paths with longer delay are more likely to have higher excess loss with respect to free space.

## IX. Conclusion

We have presented a propagation graph based model for polarized wireless channels in this paper. We also derived approximate closed form expressions for the power delay spectrum and cross polarization ratio of the indoor channel via the propagation graph formalism. A method of moments procedure for calibrating the graph model using measured data has also been presented. Our results showed that both graph model and theoretical approximation predicts accurately the power level and tail decay of the measured power delay profile for both co- and cross-polar channels. The co- and cross-polar channels decay exponentially with different and equal decay rates in the early and later parts of the power delay spectrum, respectively. We observed that the measured cross polarization ratio as a function of delay exhibit similar trend the as that obtained via simulations from the model and theoretical approximations. A transition from polarized to partially polarized and/or unpolarized state is observed in the ratio.

## Acknowledgment

This work is supported by the Cooperative Research Project VIRTUOSO, funded by Intel Mobile Communications, Keysight, Telenor, Aalborg University, and Denmark Innovation Foundation. This work was performed within the framework of the COST Action CA15104 IRACON.

## References

[1] A. S. Y. Poon and D. N. C. Tse, "Degree-of-freedom gain from using polarimetric antenna elements," *IEEE Tran. on Info. Theory*, vol. 57, no. 9, pp. 5695–5709, Sept 2011.

[2] R. G. Vaughan, "Polarization diversity in mobile communications," *IEEE Trans. Veh. Technol.*, vol. 39, no. 3, pp. 177–186, Aug 1990.

[3] J. Song, J. Choi, S. G. Larew, D. J. Love, T. A. Thomas, and A. A. Ghosh, "Adaptive millimeter wave beam alignment for dual-polarized MIMO systems," *IEEE Trans. Wireless Commun.*, vol. 14, no. 11, pp. 6283–6296, Nov 2015.

[4] J. Park and B. Clerckx, "Multi-user linear precoding for multi-polarized massive MIMO system under imperfect CSIT," *IEEE Trans. Wireless Commun.*, vol. 14, no. 5, pp. 2532–2547, May 2015.

[5] X. Su, D. Choi, X. Liu, and B. Peng, "Channel model for polarized MIMO systems with power radiation pattern concern," *IEEE Access*, vol. 4, pp. 1061–1072, 2016.

[6] M. Shafi, M. Zhang, A. L. Moustakas, P. J. Smith, A. F. Molisch, F. Tufvesson, and S. H. Simon, "Polarized MIMO channels in 3D: models, measurements and mutual information," *IEEE J. Sel. Areas Commun.*, vol. 24, no. 3, pp. 514–527, Mar 2006.

[7] 3GPP-3GPP2, "Spatial channel model for multiple input multiple output (MIMO) simulations," 3GPP, Tech. Rep., 2003.

[8] P. Kyösti, J. Meinilä, L. Hentilä, X. Zhao, T. Jämsä, C. Schneider, M. Narandzić, M. Milojević, A. Hong, J. Ylitalo, V.-M. Holappa, M. Alatossava, R. Bultitude, Y. de Jong, and T. Rautiainen, "WINNER II Channel Models," EC FP6, Tech. Rep., 2007.

[9] M. Zhu, G. Eriksson, and F. Tufvesson, "The COST 2100 Channel Model: Parameterization and Validation Based on Outdoor MIMO Measurements at 300 MHz," 2013.

[10] T. Pedersen and B. H. Fleury, "A realistic radio channel model based in stochastic propagation graphs," in *5th Conf. on Mathematical Modelling (MATHMOD 2006)*, Feb. 2006, pp. 324–331.

[11] ——, "Radio channel modelling using stochastic propagation graphs," in *IEEE ICC*, June 2007, pp. 2733–2738.

[12] T. Pedersen, G. Steinböck, and B. H. Fleury, "Modeling of reverberant radio channels using propagation graphs," *IEEE Trans. Antennas Propag.*, vol. 60, no. 12, pp. 5978–5988, Dec 2012.

[13] R. Zhang, X. Lu, Z. Zhong, and L. Cai, *A Study on Spatial-temporal Dynamics Properties of Indoor Wireless Channels*, 2011, pp. 410–421.

[14] B. Uguen, N. Amiot, and M. Laaraiedh, "Exploiting the graph description of indoor layout for ray persistency modeling in moving channel," in *EUCAP*, Mar 2012, pp. 30–34.

[15] R. Adeogun, T. Pedersen, and A. Bharti, "Transfer Function Computation for Complex Indoor Channels Using Propagation Graphs," in *IEEE International Symposium on Personal, Indoor and Mobile Radio Communications*, Sept. 2018, pp. 566–567.

[16] R. O. Adeogun, A. Bharti, and T. Pedersen, "An iterative transfer matrix computation method for propagation graphs in multi-room environments," *IEEE Antennas and Wireless Propagation Letters*, vol. 18, no. 4, pp. 616–620, April 2019.

[17] T. Pedersen, G. Steinböck, and B. H. Fleury, "Modeling of outdoor-to-indoor radio channels via propagation graphs," in *URSI General Assembly and Scientific Symposium*, Aug 2014, pp. 1–4.

[18] W. Cheng, C. Tao, L. Liu, R. Sun, and T. Zhou, "Geometrical channel characterization for high speed railway environments using propagation graphs methods," in *Intern. Conf. on Adv. Comm.n Tech.*, Feb 2014, pp. 239–243.

[19] L. Tian, V. Degli-Esposti, E. M. Vitucci, X. Yin, F. Mani, and S. X. Lu, "Semi-deterministic modeling of diffuse scattering component based on propagation graph theory," in *IEEE PIMRC*, Sept 2014, pp. 155–160.

[20] T. Zhou, C. Tao, S. Salous, Z. Tan, L. Liu, and L. Tian, "Graph-based stochastic model for high-speed railway cutting scenarios," *IET Microwaves, Antennas Propagation*, vol. 9, no. 15, pp. 1691–1697, 2015.

[21] D. K. Ntaikos, A. C. Iossifides, and T. V. Yioultsis, "Enhanced graph-theoretic channel model for performance evaluation of MIMO antennas and millimeter wave communications," in *EuCAP*, May 2015, pp. 1–4.

[22] J. Chen, X. Yin, L. Tian, and M. D. Kim, "Millimeter-wave channel modeling based on a unified propagation graph theory," *IEEE Commun. Lett.*, vol. 21, no. 2, pp. 246–249, Feb 2017.

[23] G. Steinböck, M. Gan, P. Meissner, E. Leitinger, K. Witrisal, T. Zemen, and T. Pedersen, "Hybrid model for reverberant indoor radio channels using rays and graphs," *IEEE Trans. Antennas Propag.*, vol. 64, no. 9, pp. 4036–4048, Sept 2016.

[24] L. Tian, V. Degli-Esposti, E. M. Vitucci, and X. Yin, "Semi-deterministic radio channel modeling based on graph theory and ray-tracing," *IEEE Trans. Antennas Propag.*, vol. 64, no. 6, pp. 2475–2486, June 2016.

[25] M. Gan, G. Steinböck, Z. Xu, T. Pedersen, and T. Zemen, "A hybrid ray and graph model for simulating vehicle-to-vehicle channels in tunnels," *IEEE Transactions on Vehicular Technology*, vol. 67, no. 9, pp. 7955–7968, Sept 2018.

[26] Y. Miao, T. Pedersen, M. Gan, E. Vinogradov, and C. Oestges, "Reverberant room-to-room radio channel prediction by using rays and graphs," pp. 1–1, 2018.

[27] V. Degli-Esposti, V. M. Kolmonen, E. M. Vitucci, and P. Vainikainen, "Analysis and modeling on co- and cross-polarized urban radio propagation for dual-polarized MIMO wireless systems," vol. 59, no. 11, pp. 4247–4256, Nov 2011.

[28] C. Oestges, V. Erceg, and A. J. Paulraj, "Propagation modeling of MIMO multipolarized fixed wireless channels," *IEEE Trans. Veh. Technol.*, vol. 53, no. 3, pp. 644–654, May 2004.

[29] C. Oestges, "A comprehensive model of dual-polarized channels: From experimental observations to an analytical formulation," in *Third International Conference on Communications and Networking in China*, Aug 2008, pp. 1071–1075.

[30] R. Adeogun and T. Pedersen, "Propagation graph based model for multipolarized wireless channels," in *IEEE WCNC*, April 2018.

[31] ——, "Modelling polarimetric power delay spectrum for indoor wireless channels via propagation graph formalism," in *2nd URSI Atlantic Radio Science Meeting*, May 2018.

[32] T. Pedersen, "Modeling of Path Arrival Rate for In-Room Radio Channels With Directive Antennas," *IEEE Transactions on Antennas and Propagation*, vol. 66, no. 9, pp. 4791–4805, Sep. 2018.

[33] ——, "Stochastic Multipath Model for the In-Room Radio Channel Based on Room Electromagnetics," *IEEE Transactions on Antennas and Propagation*, vol. 67, no. 4, pp. 2591–2603, April 2019.

[34] C. F. Eyring, "Reverberation time in "dead rooms"," *American Journal of Acoustic Society*, vol. 1, pp. 217 – 241, 1930.

[35] S. M. Kay, *Fundamentals of Statistical Signal Processing: Estimation Theory*. Upper Saddle River, NJ, USA: Prentice-Hall, Inc., 1993.

[36] C. Gustafson, D. Bolin, and F. Tufvesson, "Modeling the polarimetric mm-wave propagation channel using censored measurements," in *2016 IEEE Global Communications Conference (GLOBECOM)*, Dec 2016, pp. 1–6.

[37] Q. Liao, Z. Ying, and C. Gustafson, "Simulations and measurements of 15 and 28 GHz indoor channels with different array configurations," in *2017 International Workshop on Antenna Technology: Small Antennas, Innovative Structures, and Applications (iWAT)*, March 2017, pp. 256–259.

[38] C. Gustafson, K. Haneda, S. Wyne, and F. Tufvesson, "On mm-wave multipath clustering and channel modeling," vol. 62, no. 3, pp. 1445–1455, March 2014.

[39] Y. I. Wu and K. T. Wong, "Polarisation-sensitive geometric modelling of the distribution of direction-of-arrival for uplink multipaths," *IET Microwaves, Antennas Propagation*, vol. 5, no. 1, pp. 95–101, January 2011.

[40] M. Nilsson, B. Lindmark, M. Ahlberg, M. Larsson, and C. Beckman, "Measurements of the spatio-temporal polarization characteristics of a radio channel at 1800 MHz," in *IEEE 49th VTC*, vol. 1, Jul 1999, pp. 386–391 vol.1.

[41] M. Toeltsch, J. Laurila, K. Kalliola, A. F. Molisch, P. Vainikainen, and E. Bonek, "Statistical characterization of urban spatial radio channels," 2002.

[42] A. Karttunen, C. Gustafson, A. F. Molisch, J. Jrvelinen, and K. Haneda, "Censored multipath component cross-polarization ratio modeling," *IEEE Wireless Commun. Lett.*, vol. 6, no. 1, pp. 82–85, Feb 2017.